Fan-Beam Tomography and Sampling Theory

Adel Faridani

ABSTRACT. Computed tomography entails the reconstruction of a function from measurements of its line integrals. In this article we explore the question: How many and which line integrals should be measured in order to achieve a desired resolution in the reconstructed image? Answering this question may help to reduce the amount of measurements and thereby the radiation dose, or to obtain a better image from the data one already has. Our exploration leads us to a mathematically and practically fruitful interaction of Shannon sampling theory and tomography. For example, sampling theory helps to identify efficient data acquisition schemes, provides a qualitative understanding of certain artifacts in tomographic images, and facilitates the error analysis of some reconstruction algorithms. On the other hand, applications in tomography have stimulated new research in sampling theory, e.g., on nonuniform sampling theorems and estimates for the aliasing error. The focus of this article will be the application of sampling theory to the so-called fan-beam geometry. Its dual aim is an exposition of the main principles involved as well as the development of some new insights.

1. Introduction

Computed tomography (CT) entails the reconstruction of a function f from measurements of line integrals of f. Naturally, one would like to reconstruct a high-resolution image with a minimal amount of measured data. The fundamental question underlying the line of research reported here was posed in a seminal 1978 paper by A. Cormack, one of the pioneers of tomography:

> 'In practice one can make only a finite number of measurements with beams of finite width, and the question which arises is how many observations should be made, and how should they be related to each other in order to reconstruct the object' [8].

While Cormack himself proceeded with geometric arguments to discover an efficient data acquisition scheme, we will use two-dimensional sampling theory to address this question, an approach first introduced by Lindgren and Rattey [40, 55].

Sampling theory originated from the classical sampling theorem, which permits the reconstruction of a bandlimited function from its values on a regular grid or lattice. The classical sampling theorem has been extend in many directions, giving rise to a lively field of contemporary research.

It turns out that sampling theory is not only useful in identifying efficient sampling schemes for tomographic data, but among other things provides a qualitative understanding of certain artifacts and facilitates the numerical analysis of reconstruction algorithms. On the other hand, applications in tomography have stimulated research in sampling theory, for example on estimates for the aliasing error and on non-uniform sampling.

This article is organized as follows. In the next section we lay the foundation by describing the two-dimensional Radon transform which furnishes the mathematical model for tomography, as well as the classical sampling theorem. We introduce the two popular data acquisition geometries and characterize the sampling lattices for the so-called fan-beam geometry, which will serve as the focus of this article. Section 3 is devoted to some applications of the classical sampling theorem, namely identification of efficient sampling schemes and the qualitative understanding of artifacts resulting from undersampling. In § 4 we briefly describe a recent development: the use of non-equidistant periodic sampling in achieving higher resolution in fan-beam tomography. In the final section we summarize our conclusions and present a brief overview over the themes and topics of the interaction between tomography and sampling theory with references for further study.

2. Foundations

2.1. The two-dimensional Radon transform. The 2D Radon transform maps a density function f into its line integrals. Throughout this paper we will assume that $f \in C_0^\infty(\Omega)$, i.e., f is infinitely differentiable and vanishes outside the unit disk Ω of $\mathbb{R}^2$. The smoothness assumption simplifies the mathematical proofs, and although the density functions occurring in practice are not necessarily smooth, the theoretical results seem to describe the phenomena observed in practice well.

Let $\mathbb{Z}, \mathbb{R}, \mathbb{C}$ denote the integers, real and complex numbers, respectively. Let $\theta = (\cos\varphi, \sin\varphi)$ be the unit vector in $\mathbb{R}^2$ with polar angle φ, and $\theta^\perp = (-\sin\varphi, \cos\varphi)$. For $f \in C_0^\infty(\Omega)$ define its Radon transform Rf by

$$
\begin{aligned}
Rf(\varphi, s) &= \int_{-\infty}^{\infty} f(s\cos\varphi - t\sin\varphi,\ s\sin\varphi + t\cos\varphi)\, dt \\
(2.1) \qquad &= \int_{\mathbb{R}} f(s\theta + t\theta^\perp)\, dt,
\end{aligned}
$$

i.e., $Rf(\varphi, s)$ is the integral of f over the line in direction $\theta^\perp$ with signed distance s from the origin. Sometimes Rf is considered as a function of s for fixed φ. In this case we write $R_\varphi f(s)$ for $Rf(\varphi, s)$.

Observe that the parameter choices (φ, s) and $(\varphi + \pi, -s)$ lead to one and the same line. We therefore have the symmetry relation

$$
(2.2) \qquad Rf(\varphi, s) = Rf(\varphi + \pi, -s).
$$

The goal of x-ray tomography is to reconstruct an approximation to $f(x)$ from sampled values of Rf. An explanation of how the Radon transform arises as the

mathematical model for x-ray tomography is given in Quinto's article in this volume [**54**].

The Fourier transform of a function $g \in C_0^\infty(\mathbb{R}^n)$ is defined by

$$\hat{g}(\xi) = (2\pi)^{-n/2} \int_{\mathbb{R}^n} g(x) e^{-i\langle x, \xi \rangle} \, dx$$

and is extended to larger classes of functions or distributions by continuity or duality. Here $\langle x, \xi \rangle$ denotes the usual inner product in $\mathbb{R}^n$.

In particular, the Fourier transform of $R_\varphi f$ is given by

$$(R_\varphi f)^\wedge(\sigma) = (2\pi)^{-1/2} \int_{\mathbb{R}} R_\varphi f(s) e^{-is\sigma} ds.$$

The following relation between the Fourier transforms of $R_\varphi f$ and f is very useful and straightforward to verify:

$$(2.3) \qquad\qquad (R_\varphi f)^\wedge(\sigma) = (2\pi)^{1/2} \hat{f}(\sigma\theta).$$

Equation (2.3) is called the projection-slice theorem.

Discretizing the Radon transform in the variables (φ, s) of (2.1) leads to the so-called parallel-beam sampling geometry. It derives its name from the fact that keeping φ fixed and varying s leads to a collection of parallel lines.

Many medical scanners employ an x-ray source which circles around the object. This leads to the so-called fan-beam sampling geometry, where for each of a number of source positions distributed around a circle of radius $r > 1$ the integrals over rays emanating from that source position are measured. To describe this type of data collection a parametrization of lines as in (2.1) is less convenient. Instead, we introduce the divergent beam x-ray transform

$$(2.4) \qquad\qquad D_z f(\omega) = \int_0^\infty f(z + t\omega) \, dt, \quad z \in \mathbb{R}^2, \ \omega \in S^1,$$

which gives the integral of f over the ray with direction ω emanating from the source point z. Let β denote the polar angle of z, that is $z = r(\cos\beta, \sin\beta)$. We parameterize the direction ω of a ray emanating from z by $\omega = -(\cos(\alpha+\beta), \sin(\alpha+\beta))$, where α is the angle between the ray from z in direction ω and the central ray connecting z and the origin. The angle α is taken to be positive when the ray in direction ω lies to the left of the central ray when viewed from the point z. With this parametrization we have

$$D_z f(\omega) = Df(\beta, \alpha), \quad 0 \le \beta < 2\pi, \quad -\pi/2 \le \alpha \le \pi/2.$$

We extend $Df(\beta, \alpha)$ as a 2π-periodic function in α and obtain the correspondence

$$Df(\beta, \alpha) = \begin{cases} Rf(\alpha + \beta - \pi/2, r\sin\alpha), & |\alpha| < \pi/2 \\ 0 & |\alpha| \ge \pi/2 \end{cases}, \quad \alpha \in [-\pi, \pi).$$

The symmetry relation (2.2) now becomes

$$(2.5) \qquad\qquad Df(\beta, \alpha) = Df(\beta + 2\alpha + \pi, -\alpha).$$

REMARK 2.1. Since f is supported in the unit disk, its ray integrals can only be non-zero for rays intersecting the unit circle. These are the rays with $|\alpha| < \arcsin(1/r)$. Hence we could consider Df as a $2a$-periodic function in α for any a with $\arcsin(1/r) \le a \le \pi$. The choice $a = \pi$ is made here for reasons of simplicity of exposition and of consistency with the notation in [**49**]. Choosing a smaller value of a may have some advantages for computer implementations.

For readers interested in a more detailed introduction to tomography we recommend the other articles in this volume, the monographs [**45, 49**] or the introductory survey [**20**] and the references given there.

2.2. The Classical Sampling Theorem. The origin of sampling theory is the classical sampling theorem. In its simplest version it reads as follows.

THEOREM 2.2. *Let $g \in L_2(\mathbb{R})$ such that its Fourier transform $\hat{g}(\xi)$ vanishes for $|\xi| \geq b$. If $0 < h \leq \pi/b$ then*

$$g(x) = \frac{hb}{\pi} \sum_{l \in \mathbb{Z}} g(hl) \operatorname{sinc}(b(x - hl)),$$

where $\operatorname{sinc}(t) = \frac{\sin t}{t}$. The series converges in L_2 as well as uniformly.

REMARK 2.3. The term sinc stands for 'sinus cardinalis', and the series is called 'cardinal series'. The following observations will be useful for generalizing the theorem; cf. Theorem 2.7 below.

(1) The theorem permits recovery of g from its values on a subgroup $\mathbf{L} = h\mathbb{Z}$ of $\mathbb{R}$. $\mathbf{L}$ is also called a lattice.
(2) The set $\mathbf{L}^{\perp} = \{2\pi l/h, \ l \in \mathbb{Z}\}$ satisfies $e^{iy\eta} = 1$ for all $y \in \mathbf{L}$, $\eta \in \mathbf{L}^{\perp}$ and is called the dual or reciprocal lattice of $\mathbf{L}$. According to the hypothesis of Theorem 2.2 the support of $\hat{g}$ is contained in the closure of the set $K = [-b, b)$. The density condition $h \leq \pi/b$ is therefore equivalent to the condition that the translates $K + \eta$, $\eta \in \mathbf{L}^{\perp}$ are mutually disjoint.
(3) Note that the function $s(x) = \operatorname{sinc}(bx)$ is up to a multiplicative constant equal to the inverse Fourier transform $\tilde{\chi}_K$ of the indicator function χ_K of $K = [-b, b)$. Recall that $\chi_K(\xi) = 1$ for $\xi \in K$ and $\chi_K(\xi) = 0$ otherwise. We have

$$(2.6) \qquad \tilde{\chi}_K(x) \ = \ (2\pi)^{-1/2} \int_{-b}^{b} e^{ix\xi} \, d\xi \ = \ \sqrt{\frac{2}{\pi}} \frac{\sin bx}{x} \ = \ \sqrt{\frac{2}{\pi}} \, b \operatorname{sinc}(bx).$$

The sampling theorem is closely related to the *Poisson summation formula*, which is a fundamental tool for all results which will be discussed in this paper. Its one-dimensional version reads as follows.

THEOREM 2.4 (Poisson summation formula for $\mathbb{R}$). *Let $h > 0$, $z, \sigma \in \mathbb{R}$, and $g \in C(\mathbb{R})$ such that $|g(x)| \leq C(1 + |x|)^{-1-\epsilon}$, and $|\hat{g}(\xi)| \leq C(1 + |\xi|)^{-1-\epsilon}$ for some $C > 0$, $\epsilon > 0$. Then*

$$(2.7) \qquad (2\pi)^{-1/2} h \sum_{l \in \mathbb{Z}} g(z + hl) \, e^{-i\sigma(z+hl)} = \sum_{l \in \mathbb{Z}} \hat{g}(\sigma + 2\pi l/h) \, e^{iz2\pi l/h}.$$

For a proof see, e.g., [**24**, Theorem (8.36)]. The result holds also under less restrictive hypotheses and in a very general setting; see [**26**, p. 217].

The sampling theorem can be formally derived from (2.7) as follows. Let $z = 0$ in (2.7). If $\hat{g}(\xi)$ vanishes for $|\xi| \geq b$ and $h \leq \pi/b$, then the right-hand side of (2.7) simplifies to $\hat{g}(\sigma)$ for $|\sigma| \leq b$. Now take the inverse Fourier transform

$$g(x) = (2\pi)^{-1/2} \int_{-b}^{b} \hat{g}(\sigma) \, e^{ix\sigma} \, d\sigma,$$

replace in the integral $\hat{g}(\sigma)$ by the left-hand side of (2.7) and use (2.6).

Another important application of the Poisson summation formula consists in error estimates for numerical integration with the trapezoidal rule. Assume for example that $\hat{g}(\sigma) = (2\pi)^{-1/2} \int_{\mathbb{R}} g(x) e^{-i\sigma x} \, dx$ is to be approximated by

$$\hat{g}(\sigma) \simeq (2\pi)^{-1/2} h \sum_{l \in \mathbb{Z}} g(hl) e^{-i\sigma hl}.$$

Letting $z = 0$ in (2.7) we obtain the following expression for the integration error:

$$(2\pi)^{-1/2} h \sum_{l \in \mathbb{Z}} g(hl) e^{-i\sigma hl} \; - \; \hat{g}(\sigma) \; = \; \sum_{l \neq 0} \hat{g}(\sigma + 2\pi l/h).$$

The classical sampling theorem is fundamental for signal processing, has been generalized in many directions, and given rise to the field of sampling theory. Readers seeking more information on sampling theory will find ample material in survey articles including [**1, 7, 28, 34**], monographs such as [**29, 41, 60**], and collections of research articles, e.g., [**3, 4, 30, 42**].

2.3. Sampling lattices for the divergent beam transform. We have seen that $Df(\beta, \alpha)$ is a function with domain $[0, 2\pi) \times [-\pi, \pi)$. For the subsequent analysis it is more convenient to transform this domain to $[0, 1)^2$ by means of the change of variables

$$(2.8) \qquad \begin{aligned} g(s,t) &= Df(\beta, \alpha) \\ (s,t) &\in [0,1)^2, \quad (\beta, \alpha) \in [0, 2\pi) \times [-\pi, \pi) \\ s &= \frac{\beta}{2\pi}, \quad t = \frac{\alpha}{2\pi} + \frac{1}{2}, \end{aligned}$$

that is, we will henceforth consider the function

$$(2.9) \qquad g(s,t) = Df(2\pi s, 2\pi t - \pi), \quad (s,t) \in [0,1)^2.$$

This will allow us to directly use the theory and algorithms developed in [**18**, §4].

The subsequent analysis of sampling and resolution will make use of Fourier analysis. This requires both the domain of g as well as the sampling sets to have a group structure. Equipped with addition modulo 1 the interval $[0, 1)$ becomes a group, called the circle group, which we denote by $\mathbb{T}$. Then the domain of g may be identified with the group $\mathbb{T}^2$, called the torus group. The Fourier transform of g is given by

$$\hat{g}(k,m) = \int_0^1 \int_0^1 g(s,t) \, e^{-2\pi i (ks + mt)} \, ds \, dt, \quad (k,m) \in \mathbb{Z}^2.$$

Using the notation $z = (s,t)$, $\zeta = (k,m)$, $\langle z, \zeta \rangle = sk + tm$, this can be written as

$$\hat{g}(\zeta) = \int_{\mathbb{T}^2} g(z) \, e^{-2\pi i \langle z, \zeta \rangle} \, dz, \quad \zeta \in \mathbb{Z}^2.$$

The inverse Fourier transform in this setting is given by

$$\begin{aligned} \tilde{G}(s,t) &= \sum_{k \in \mathbb{Z}} \sum_{m \in \mathbb{Z}} G(k,m) \, e^{2\pi i (ks + mt)} \\ &= \int_{\mathbb{Z}^2} G(\zeta) \, e^{2\pi i \langle z, \zeta \rangle} \, d\zeta, \end{aligned}$$

with $z = (s,t) \in \mathbb{T}^2$, $\zeta = (k,m) \in \mathbb{Z}^2$, and $d\zeta$ denoting the counting measure on $\mathbb{Z}^2$.

The task of fan-beam tomography is to reconstruct f from finitely many measurements of g. We require the set of all points (s, t) where g is measured to be a (possibly shifted) finite subgroup of $\mathbb{T}^2$. We call a finite subgroup $\mathbf{L}$ of $\mathbb{T}^2$ a lattice or sometimes a sampling lattice. Every lattice $\mathbf{L}$ in $\mathbb{T}^2$ has a corresponding 'reciprocal lattice' $\mathbf{L}^\perp$ in the Fourier domain $\mathbb{Z}^2$. $\mathbf{L}^\perp$ is the set of all $\eta \in \mathbb{Z}^2$ such that $e^{2\pi i \langle y, \eta \rangle} = 1$ for all $y \in \mathbf{L}$.

In order to systematically investigate sampling on $\mathbb{T}^2$ we need to characterize and parametrize all lattices. Fortunately such a characterization of the finite subgroups of $\mathbb{T}^2$ is available in the literature. Let $|\mathbf{L}|$ denote the number of elements of a lattice $\mathbf{L}$ and let $[x]$ denote the fractional part of a real number x, i.e., $[x] \in [0, 1)$ and $x - [x] \in \mathbb{Z}$.

PROPOSITION 2.5. If $\mathbf{L}$ is a finite subgroup of $\mathbb{T}^2$, then there exists a unique non-singular lower triangular 2×2 matrix W such that

(i) As a set, $\mathbf{L} = [W\mathbb{Z}^2]$, and $\mathbf{L}^\perp = W^{-T}\mathbb{Z}^2$.

(ii) $|\mathbf{L}| = |\det W|^{-1}$

(iii) The matrix W^{-T} has Hermite normal form, i.e. W^{-T} is an upper triangular matrix

$$(2.10) \quad W^{-T} = \begin{pmatrix} P & -N \\ 0 & Q \end{pmatrix} \quad \text{with } N, P, Q \in \mathbb{Z}, \ P, Q > 0, \ 0 \leq N \leq P - 1.$$

W and W^{-T} are called generator matrices of $\mathbf{L}$ and $\mathbf{L}^\perp$, respectively.

Proof: This is the two-dimensional case of Proposition 4.2 in [**18**], which in turn is based on [**50**, pp. 125-126, 131-132] and [**51**, Theorems II.2, II.3]. $\square$

From Proposition 2.5 we conclude the following. Any sampling lattice $\mathbf{L} = \mathbf{L}(N, P, Q)$ is characterized by three integers N, P, Q such that $P, Q > 0$, $0 \leq N \leq P - 1$, the generator matrix W is given by

$$W = \begin{pmatrix} 1/P & 0 \\ N/(PQ) & 1/Q \end{pmatrix},$$

and

$$
\begin{aligned}
(2.11) \quad \mathbf{L} &= [W\mathbb{Z}^2] \\
&= \{(s_j, t_{jl}) : \ s_j = j/P, \ t_{jl} = [(l + Nj/P)/Q], \\
&\quad j = 0, \dots, P-1, \ l = 0, \dots, Q-1\}.
\end{aligned}
$$

Furthermore, the reciprocal lattice is given by

$$(2.12) \quad \mathbf{L}^\perp(N, P, Q) = \{(Pk_1 - Nk_2, \ Qk_2), \ k_1, k_2 \in \mathbb{Z}\}.$$

Going back for a moment to the (β, α) coordinates we see that sampling lattices for fan-beam tomography have the following structure:

- There are P source positions $z_j = r(\cos \beta_j, \sin \beta_j)$ corresponding to the equidistant angles

$$\beta_j = 2\pi j/P, \quad j = 0, \dots, P - 1.$$

- For each of these source positions Q integrals over rays corresponding to an equidistant set of angles α_{jl} with spacing $2\pi/Q$ are measured.

- This collection of equiangular rays is shifted by an amount which varies with the angle β_j, so that the α-values corresponding to the angle β_j are given by

$$\alpha_{jl} = -\pi + 2\pi[(l + Nj/P)/Q], \quad 0 \le l \le Q - 1$$

  where the parameter $N \in \mathbb{Z}$, $0 \le N \le P - 1$ determines the shifting pattern.

Hence every sampling lattice $\mathbf{L} = \mathbf{L}(N, P, Q)$ is characterized by its number of source positions P, the number Q of equiangularly spaced rays in each fan, and the shift parameter N. The total number of samples equals PQ.

The most frequently used lattice is the *standard lattice*

$$\mathbf{L}_S = \mathbf{L}(0, P, Q) = \{(s_j, t_l) : s_j = j/P, \ t_l = l/Q, \ j = 0, \ldots, P - 1, \ l = 0, \ldots Q - 1\}$$

which is obtained by letting $N = 0$.

We wish to apply Shannon sampling theory in order to find the best sampling lattices. In order to do this we need to state the Poisson summation formula and the classical sampling theorem for functions defined on $\mathbb{T}^2$.

THEOREM 2.6 (Poisson summation formula for $\mathbb{T}^2$). *Let $z \in \mathbb{T}^2$, $\zeta \in \mathbb{Z}^2$, $\mathbf{L} = \mathbf{L}(N, P, Q)$ be a sampling lattice and $g \in C^\infty(\mathbb{T}^2)$. Then*

$$(2.13) \qquad \frac{1}{PQ} \sum_{y \in \mathbf{L}} g(z + y) e^{-2\pi i \langle z + y, \zeta \rangle} = \sum_{\eta \in \mathbf{L}^\perp} \hat{g}(\zeta + \eta) e^{2\pi i \langle z, \eta \rangle}.$$

The classical sampling theorem for this setting reads as follows.

THEOREM 2.7. *Let $g \in C^\infty(\mathbb{T}^2)$, $\mathbf{L} = \mathbf{L}(N, P, Q)$ a sampling lattice and K be a finite subset of $\mathbb{Z}^2$ such that its translates $K + \eta$, $\eta \in \mathbf{L}^\perp$ are disjoint. Let χ_K denote the indicator function of K, i.e., $\chi_K(\zeta) = 1$ if $\zeta \in K$ and $\chi_K(\zeta) = 0$ otherwise. For $z \in \mathbb{T}^2$ define*

$$(2.14) \qquad Sg(z) = \frac{1}{PQ} \sum_{y \in \mathbf{L}} \tilde{\chi}_K(z - y) g(y).$$

Then

$$(2.15) \qquad |g(z) - Sg(z)| \quad \le \quad 2 \int_{\mathbb{Z}^2 \backslash K} |\hat{g}(\zeta)| \, d\zeta.$$

For a proof see, e.g., [17] or [45, pp. 62–64]. In these references the domain of the function g is different, but the proof is readily transferred to the present setting. The key idea is to start out with the observation

$$|g(z) - Sg(z)| \le \int_{\mathbb{Z}^2} |\hat{g}(\zeta) - \widehat{Sg}(\zeta)| \, d\zeta,$$

split the integral into integrals over K and $\mathbb{Z}^2 \backslash K$, observe that $\widehat{Sg}$ vanishes outside K, and estimate the integral over K using the Poisson summation formula and the disjointness of the translates of K under elements of $\mathbf{L}^\perp$.

Observe that if $\hat{g}$ vanishes outside of K then $g = Sg$, i.e., g can be recovered exactly from its samples on the lattice $\mathbf{L}$.

The right-hand side of (2.15) provides an estimate for the so-called aliasing error. If g as in (2.9) is the divergent beam transform of a function with compact support, then the Fourier transform $\hat{g}$ cannot have compact support and an aliasing error will always be present.

3. Applications of the Classical sampling theorem.

In this section we illustrate some of the applications of the classical sampling theorem, namely the identification of efficient sampling schemes and the qualitative understanding of artifacts. Our presentation will focus on the fan-beam geometry. An analogous discussion for the parallel-beam geometry can be found in [21].

3.1. Identification of efficient sampling schemes.
Theorem 2.7 indicates what needs to be done in order to find efficient sampling schemes for tomography, i.e., when $g(s,t) = Df(2\pi s, 2\pi t - \pi)$. First we need to find a suitable set K so that the right-hand side of (2.15) is sufficiently small. Then we need to identify lattices $\mathbf{L}(N, P, Q)$ as sparse as possible but such that the translated sets $K + \eta$, $\eta \in \mathbf{L}^\perp$ are disjoint.

The set K will of course depend on the function f. The crucial parameter turns out to be a cut-off frequency b such that $|\hat{f}(\xi)|$ is negligible for $|\xi| > b$, in the sense that the integral $\int_{|\xi|>b} |\hat{f}(\xi)| d\xi$ is sufficiently small. The parameter b may be viewed as an 'essential bandwidth' of f. In [46] it is shown that then $|\hat{g}(k, m)|$ will be small for $|k - m| \geq rb$. On the other hand, it follows from [52, Theorem 2] that due to f being supported in the unit disk, $|\hat{g}(k, m)|$ is small and decays exponentially with increasing k in the region $r|k| \geq \vartheta^{-1}|k-m|$, where the 'safety parameter' ϑ satisfies $0 < \vartheta < 1$ and can usually be chosen very close to 1. Combining these estimates and leaving some safety margin near the origin (cf. [25]) leads us to the set
(3.1)
$$K(\vartheta, b) = \left\{ (k, m) \in \mathbb{Z}^2 : \ |k - m| < rb, \ r|k| < \vartheta^{-1} \max(|k - m|, (1 - \vartheta)rb) \right\};$$

see Figure 1. In this connection it is important to note that the only assumption made about f when determining K is the essential bandwidth b. If f has additional properties the essential support of $\hat{g}$ may be smaller than $K(\vartheta, b)$. For example, if f is rotationally symmetric, then $\hat{g}(k, m) = 0$ for $|k| > 0$.

The crucial feature both for finding efficient sampling schemes and for understanding some of the artifacts caused by undersampling is the particular, non-convex shape of K. It stems from the fact that the function f has compact support.

The next step in applying Theorem 2.7 is to find conditions for the lattice parameters N, P, Q such that the translated sets $K(\vartheta, b) + \eta$, $\eta \in \mathbf{L}^\perp(N, P, Q)$ are disjoint. This is a requirement for the reciprocal lattice to be sparse which means that the sampling lattice itself must be sufficiently dense.

We begin with the standard lattice, i.e., $N = 0$. According to (2.12) the reciprocal lattice is given by

$$\mathbf{L}_S^\perp \ = \ \mathbf{L}^\perp(0, P, Q) \ = \ \{(Pk_1, \ Qk_2), \ \ k_1, k_2 \in \mathbb{Z}\}.$$

In particular, the points $\eta_1 = (0, Q)$, $\eta_2 = (P, 0)$, and $\eta_3 = (P, Q)$ are elements of $\mathbf{L}_S^\perp$. Because of the symmetries of $K(\vartheta, b)$ and $\mathbf{L}_S$ the sets $K(\vartheta, b) + \eta$, $\eta \in \mathbf{L}_S^\perp$ will be disjoint if and only if the sets $K(\vartheta, b) + \eta_i$, $i = 1, 2, 3$, do not intersect $K(\vartheta, b)$. The sets $K(\vartheta, b) + (0, Q)$ and $K(\vartheta, b) + (P, 0)$ will be disjoint from $K(\vartheta, b)$ if and only if $Q \geq 2rb$ and $P \geq \max \left(2rb/(1 + \vartheta r), (2 - \vartheta)b/\vartheta\right)$, respectively. Usually ϑ is chosen sufficiently close to 1 for the latter condition to simplify to $P \geq 2rb/(1+\vartheta r)$. In this case it turns out that for the minimal choice
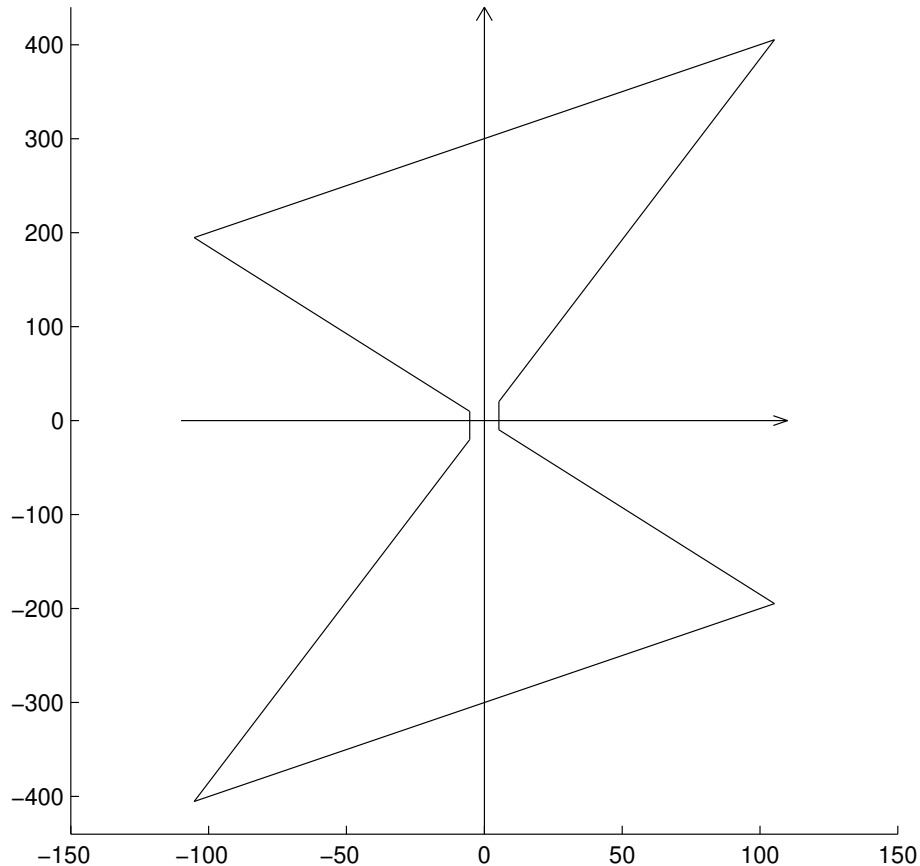
(3.2)
$$P = \frac{2rb}{1 + \vartheta r}, \qquad Q = 2rb$$

FIGURE 1.   The set $K(\vartheta, b)$ of (3.1) for $\vartheta = 0.95$, $b = 100$, and $r = 3$. The coordinates of the four outer corners are $\pm(b/\vartheta,\ (1+\vartheta r)b/\vartheta)$ and $\pm(b/\vartheta,\ (1-\vartheta r)b/\vartheta)$. The coordinates of the four corners near the origin equal $(1 - \vartheta)$ times the coordinates of the outer corners. In the case $\vartheta = 1$ these four inner corners coincide at the origin, resulting in the set K given in [**46**] and [**49**, p. 75].

the set $K(\vartheta, b) + (P, Q)$ is also disjoint from $K(\vartheta, b)$, so that all sets $K(\vartheta, b) + \eta$, $\eta \in \mathbf{L_S^\perp}$ are disjoint; see Figure 2. From this figure we can also see that keeping P fixed and slightly increasing Q would move the set $K(\vartheta, b) + (P, Q)$ higher and may lead to its intersection with $K(\vartheta, b)$. Thus the sampling conditions would be violated in spite of having sampled more data. This phenomenon comes from the non-convexity of $K(\vartheta, b)$ and will be discussed further in §3.3 below. Avoiding this intersection of sets requires further restrictions on the choice of Q as long as $P < 2b/\vartheta$. We obtain the following conditions.

$$\text{If } \max\left(\frac{2rb}{1 + \vartheta r},\ (2 - \vartheta)b/\vartheta\right)\ \leq\ P\ <\ 2b/\vartheta,$$

(3.3)   then choose either $2rb\ \leq\ Q\ \leq\ (1 + \vartheta r)P$ or $Q\ \geq\ 2rb + P$.

The conditions simplify considerably if $P \geq 2b/\vartheta$, since then the sets $K(\vartheta, b)$ and $K(\vartheta, b) + (P, Q)$ cannot intersect. Hence the sets $K + \eta$, $\eta \in \mathbf{L}_\mathbf{S}^\perp$ will be disjoint if

$$(3.4) \qquad\qquad P \geq 2b/\vartheta, \quad Q \geq 2rb.$$

Together the conditions (3.3) and (3.4) form a necessary and sufficient set of sampling conditions for the standard lattice. For comparison of these conditions with earlier results in the literature it is sometimes helpful to rewrite them in terms of the angular increments $\Delta\beta = 2\pi/P$ and $\Delta\alpha = 2\pi/Q$.
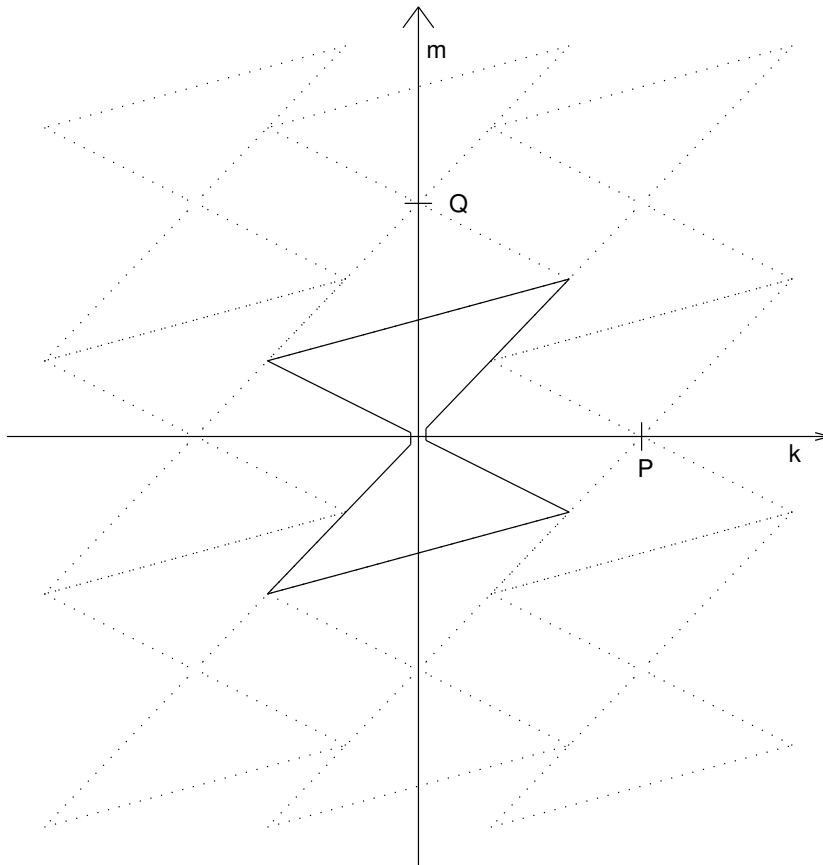

FIGURE 2.   The translated sets $K(\vartheta, b) + \eta$ for the standard lattice in case of $P = \frac{2rb}{1 + \vartheta r}$, $Q = 2rb$, $b = 100$, $r = 3$, $\vartheta = 0.95$.

The translated sets in Figure 2 do not appear to be packed as densely as possible. Another arrangement corresponding to a different lattice may result in a denser packing, giving a denser reciprocal lattice and therefore a sparser sampling lattice. However, it is apparent from letting $k_1 = 1$, $k_2 = 0$ in (2.12) that the point $\eta = (P, 0)$ always belongs to $\mathbf{L}^\perp(N, P, Q)$. Hence for every sampling lattice P needs to be chosen no smaller than $\max(2rb/(1 + \vartheta r), (2 - \vartheta)b/\vartheta)$, since otherwise the sets $K(\vartheta, b)$ and $K(\vartheta, b) + (P, 0)$ would intersect. Hence the standard lattice is optimal in the sense that it allows for parameter choices with a

minimal number of source positions. Since the total number of measurements is PQ, other lattices can only be more efficient overall by allowing values of Q less than $2rb$ or by exploiting the symmetry (2.5). On the other hand the choice $k_1 = N/\gcd(P, N)$, $k_2 = P/\gcd(P, N)$ in (2.12) reveals that the reciprocal lattice always contains the point $\eta = (0, QP/\gcd(P, N))$. This yields the necessary condition $Q \geq 2rb\gcd(P, N)/P$. If $\gcd(P, N) < P$ this would allow for values of Q smaller than $2rb$. However, the above condition is only necessary but in general not sufficient to avoid overlap of the translated sets $K + \eta$, $\eta \in \mathbf{L}^\perp$.

Natterer [**46**] showed that in the case $\vartheta = 1$ a lattice $\mathbf{L}$ of optimal sparsity is given if b and rb are integers and the generator matrix of the reciprocal lattice has the form

$$(3.5) \qquad W^{-T} = \begin{pmatrix} b & 0 \\ (1-r)b & 2rb \end{pmatrix}, \quad b, rb \in \mathbb{Z}.$$

(see also [**47**] and [**49**, p. 77]). According to Proposition 2.5 there exists a unique matrix of the form (2.10) that generates the same reciprocal lattice. This matrix can be found using an algorithm similar to the one described in [**6**]. This yields the lattice parameters

$$(3.6) \qquad Q = \gcd((r-1)b, 2rb), \quad P = 2rb^2/Q, \quad N = -\mathrm{mod}(nb, -P),$$

where the integer n is found by the relation $m2rb - n(r-1)b = Q$, with $m \in \mathbb{Z}$, and $\mathrm{mod}(nb, -P)$ denotes the unique integer in $[1 - P, \, 0]$ which differs from nb by a multiple of P. For example, let $r = 3$ and $b = 100$. Then $Q = \gcd(200, 600) = 200$, $P = 300$, $m = 0$, $n = -1$, $N = 100$. In comparison, the sampling conditions for the standard lattice require at least $P = 2rb/(1 + r) = 150$ and $Q = 2rb = 600$. So the total number PQ of lattice points for the efficient lattice is in this case $2/3$ of the number of points required for the standard lattice. In general this ratio equals $(1 + r)/(2r)$, which approaches 1 for $r \to 1$ and $1/2$ in the limit $r \to \infty$. Our numerical experiments indicate that the set K may be slightly too small in the case $\vartheta = 1$. In case of $\vartheta < 1$ the values of P and N have to be slightly increased for the efficient lattice, leaving the ratio P/N unchanged.

Figure 3 shows the case of (nearly) optimally sparse sampling with the efficient lattice, for $b = 100$, $r = 3$, $\vartheta = 0.95$, $P = 330$, $N = 110$, $Q = 200$. It obtains the same theoretical resolution (as determined by the bandwidth b) as the standard lattice with approximately 73% of the amount of data required for the standard lattice.

Practical drawbacks of the efficient lattice include the presence of the dynamic detector shift since $N \neq 0$ which may be inconvenient to realize in practice, and that for some values of r and b the value for P in (3.6) can become very large and the value for Q very small. We will disregard these difficulties for the moment and explore if indeed accurate reconstructions can be obtained from efficiently sampled data.

3.2. Reconstruction. There are at least two ways in which to approach the reconstruction of images from the sampled data. First, one could use the sampled data directly as input for a reconstruction algorithm, for example the filtered backprojection algorithm. Second, one could first interpolate the sampled data to a denser lattice using the sampling theorem, and then reconstruct from these interpolated data. In the parallel-beam case it was shown in [**38, 17, 22**] that filtered backprojection can be used directly, even with efficiently sampled data, although
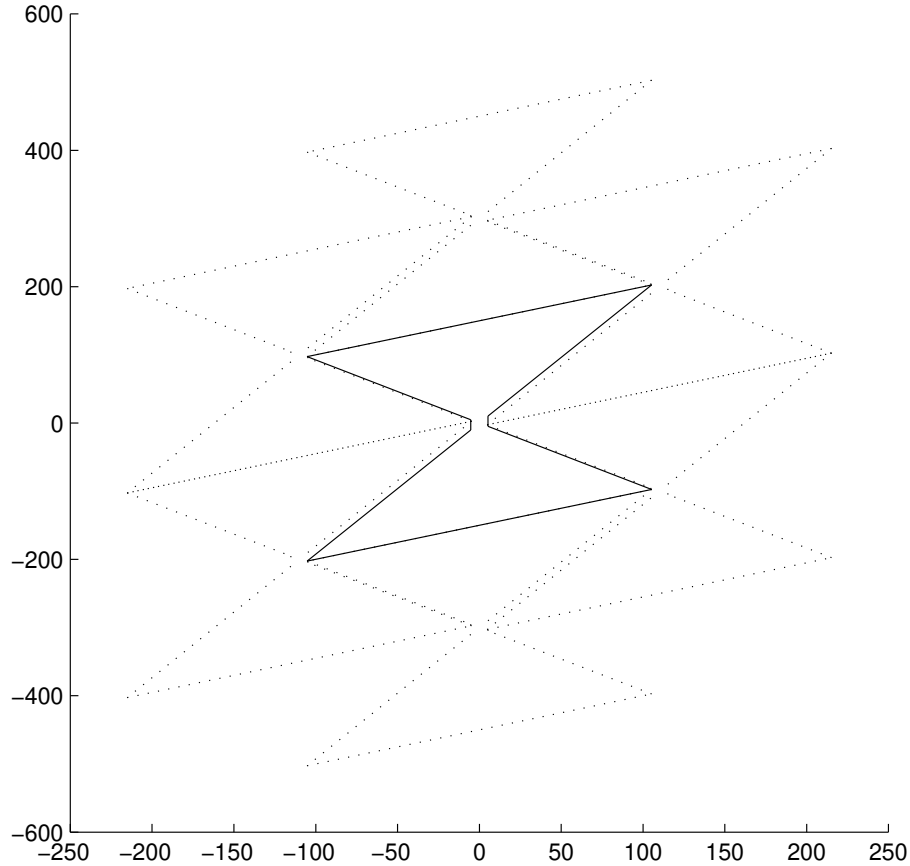
FIGURE 3.   Some of the translated sets $K(\vartheta, b) + \eta$, $\eta \in$ $\mathbf{L}^{\perp}(N, P, Q)$ for the efficient lattice in case of $r = 3$, $b = 100$, $\vartheta = 0.95$, $N = 110$, $P = 330$, $Q = 200$.

experiments in [**16**] indicate that the second approach may be slightly better. We now investigate this situation for the fan-beam geometry and compare using the filtered backprojection algorithm directly with the method of first bandlimiting and interpolating the data onto a denser lattice and only then reconstructing with the filtered backprojection algorithm. We use the version of the fan-beam filtered back-projection algorithm as described in [**45**] or [**35**], with a convolution kernel similar to [**35**, §3.4.1], but replace the straight ramp filter $h(t)$ used in [**35**, p. 82] with the Shepp-Logan kernel as given in [**45**, p. 111]. The algorithm used for bandlimiting and interpolating the data is described in [**18**, §4].

We will use simulated data from a very simple object for our investigation, namely the function

$$(3.7) \qquad\qquad f(y) = \left(1 - 100|y - y_0|^2\right)_+^3, \quad y_0 = (0.4,\, 0.7)$$

where the $+$ symbol indicates that $f(y) = 0$ whenever $(1 - 100|y - y_0|^2) < 0$. The function $f(y)$ is supported in the region $|y - y_0| \le 0.1$. Since f is quite smooth, it is essentially bandlimited and therefore provides a good test for our theory. Choosing

a cut-off frequency $b = 100$ will be sufficient for a good reconstruction. Since f is known analytically, we can use not only the visual impression of the images but also the discrete relative l_2-error as a measure for the accuracy of the reconstruction. If $I(x_n, y_m)$ is the reconstructed image, the relative l_2-error is given by

$$E = \left(\frac{\sum_{n,m} |f(x_n, y_m) - I(x_n, y_m)|^2}{\sum_{n,m} |f(x_n, y_m)|^2} \right)^{\frac{1}{2}}.$$

The upper left image in Figure 4 shows the direct reconstruction with the filtered backprojection algorithm from data sampled on the standard lattice with $b = 100$, $r = 3$, $P = \text{ceil}(2rb/(1 + \vartheta r)) = 156$, $N = 0$, and $Q = 2rb = 600$. The discrete convolution occurring in the algorithm is computed on a very dense grid with stepsize $H = \pi/(8Q) = \pi/4800$ in order to suppress errors stemming from the interpolation step of the algorithm; cf. [**21**, §6], [**22**]. The reconstruction is computed on a 256×256 grid. The maximum of $f(x)$ is 1, but since we want to study small artifacts the display window is such that values below -0.01 are rendered black and values above 0.01 are rendered white. The relative l_2-error is about 5.4%. The lower left image shows the reconstruction after interpolating the data first onto the denser lattice with $P = 274$, $Q = 892$, $N = 0$ and then using the filtered backprojection algorithm. The interpolation was done using the sampling theorem and the algorithm described in [**18**, §4]. It computes the Fourier transform of the data inside K, sets it to zero outside K, and then computes the data on the denser lattice using an Inverse Fast Fourier Transform. The relative l_2-error is now about 2.4%, less than half of the error of the direct reconstruction. The difference between the two methods of reconstruction is even more pronounced in case of the efficient lattice. The upper right image in Figure 4 shows the direct reconstruction from efficiently sampled data with $P = 330$, $Q = 200$, $N = 110$, and the other parameters as above. There are strong artifacts and the relative l_2-error is now about 52%. The lower right image shows the reconstruction with prior interpolation onto the standard lattice with parameters $P = 274$, $Q = 892$, $N = 0$, and the discrete convolution computed on a grid with a stepsize of $H = \pi/4906$. The relative l_2-error is about 2.4%, almost exactly the same as for the reconstruction in the lower left image. This experiment indicates that accurate reconstruction from efficiently sampled data is possible if the data are first bandlimited to K and then interpolated onto a denser grid. On the other hand, the filtered backprojection algorithm in its usual form does not appear to achieve the theoretically possible resolution when reconstructing directly from the data without prior interpolation to a denser grid. A heuristic explanation for this behavior could be as follows: The change of variables from parallel-beam to fan-beam yields for the convolution step of the algorithm a cut-off frequency $b' = |x - z(\beta)|b$ which depends on the reconstruction point x and the source location $z(\beta) = r(\cos(\beta), \sin(\beta))$. In order to obtain a fast algorithm b' is replaced by a constant b_c; cf. [**45**, p. 113]. It appears that in order to obtain the desired resolution b_c should not be smaller than the maximum of $|x - z(\beta)|b$, i.e., $(r + 1)b$. On the other hand, the values of P and Q used for the reconstruction should be large enough for the numerical integrations occurring in the algorithm to be accurate for such a value of b_c. The reconstructions from efficiently sampled data presented in [**46**] where performed with a modified filtered backprojection algorithm (see [**46**, Eq. (4.7)]) which apparently avoided replacing b' by a constant, but may be slow as a consequence. Since the bandlimiting
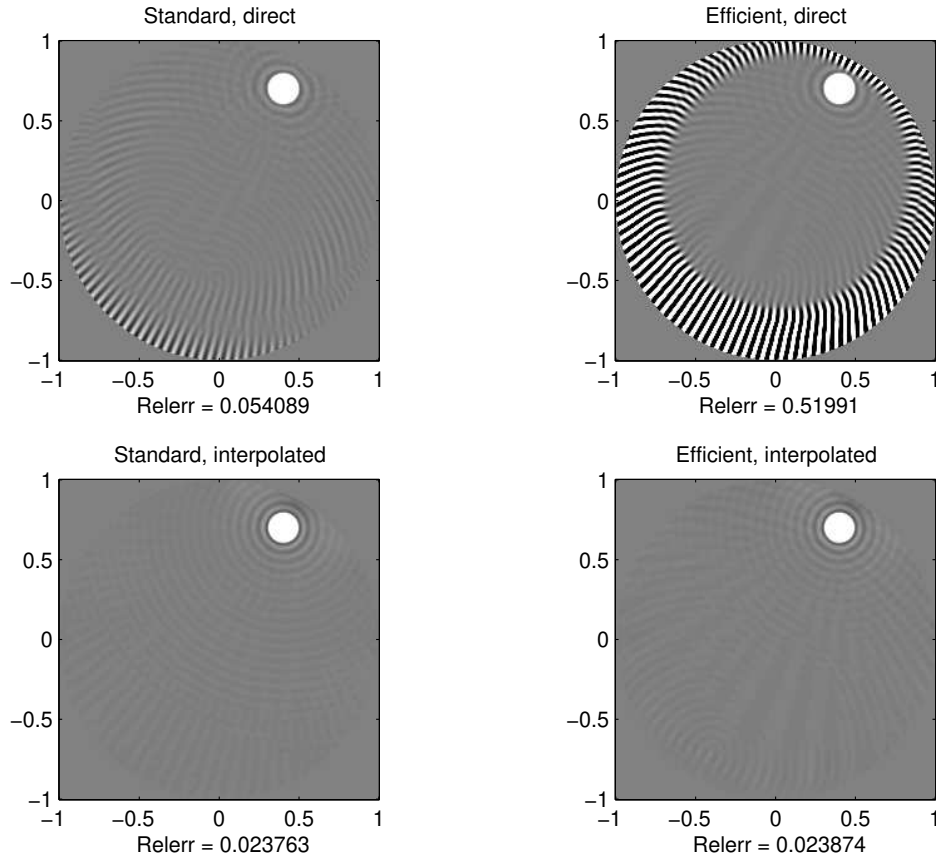
FIGURE 4.   Reconstructions of the function $f(x)$ of (3.7). All
reconstructions are computed with $b = 100$, $r = 3$, and displayed
on a 256×256 grid. The function takes values between 0 and 1,
but in order to highlight small artifacts the display is such that
values smaller than -0.01 are rendered black and values larger
than 0.01 are rendered white. Upper row: Direct reconstructions
with filtered backprojection algorithm. Upper left: Data sampled
on the standard lattice with $P = 156$, $N = 0$, $Q = 600$. Upper
right: Efficient lattice with $P = 330$, $N = 110$, $Q = 200$. Lower
row: Reconstructions after bandlimiting the data to $K(\vartheta, b)$, $\vartheta =$
0.95, and then interpolating onto a denser standard lattice with
$P = 274$, $N = 0$, $Q = 892$ prior to reconstruction with filtered
backprojection. Lower left: Original data sampled on standard
lattice as in upper left. Lower right: Original data sampled on
efficient lattice as in upper right.

and interpolation by the sampling theorem is much faster than reconstruction with
the filtered backprojection algorithm, adding this step does not lead to a significant
slowdown of the reconstruction.

3.3. Qualitative understanding of artifacts from undersampling. Now we investigate the effects of undersampling, that is, of violating the sampling conditions requiring the translates $K + \eta$, $\eta \in \mathbf{L}^\perp$ to be disjoint. Consider the following numerical experiments. Figure 5 again shows various reconstructions of the func-
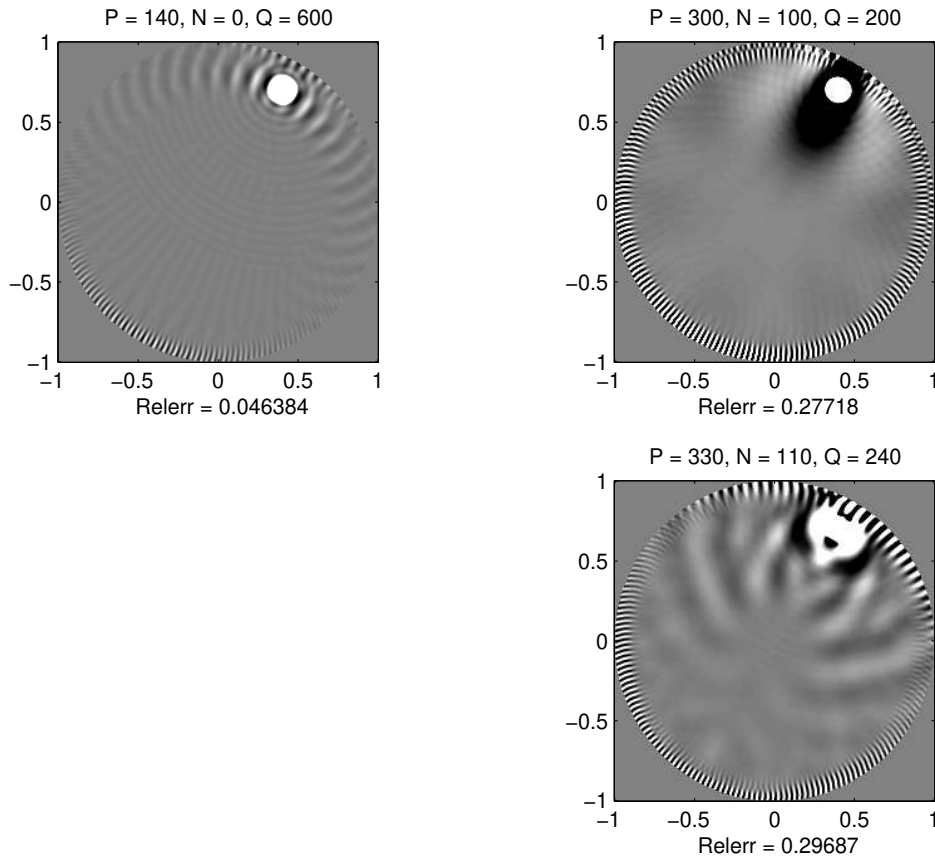

FIGURE 5. Artifacts resulting from undersampling. The function to be reconstructed is $f(x)$ from (3.7). All reconstructions are computed with $b = 100$, $r = 3$, and displayed on a 256×256 grid such that values less than -0.01 are rendered black and values greater than 0.01 are rendered white. Top row: Effects of P being too small. Top left: Reconstruction from standard lattice with $P = 140$ instead of 156. Top right: Reconstruction from efficient lattice with P reduced to 300 from 330. Bottom right: Reconstruction from efficient lattice with Q *increased* from 200 to 240.

tion $f(x)$ given in (3.7), from fan beam data with source radius $r = 3$ and cut-off frequency $b = 100$.

The upper left picture shows a reconstruction with the standard lattice with $Q = 600$ and P reduced to 140 from the value of 156 required by the sampling conditions (3.3) for $r = 3$, $b = 100$, and $\vartheta = 0.95$. This reduction of P by about

10% results in a relative l_2-error of about 4.6%. The upper right picture shows the corresponding case for the efficient lattice, where P has been reduced by about 10% from 330 to 300. The resulting artifacts are much stronger, resulting in a relative error of about 28%. The picture in the lower right shows an at first glance surprising result. Here we used the efficient lattice and *increased* the parameter Q from 200 to 240. In spite of having sampled more data we obtain strong artifacts and a relative error of almost 30%.
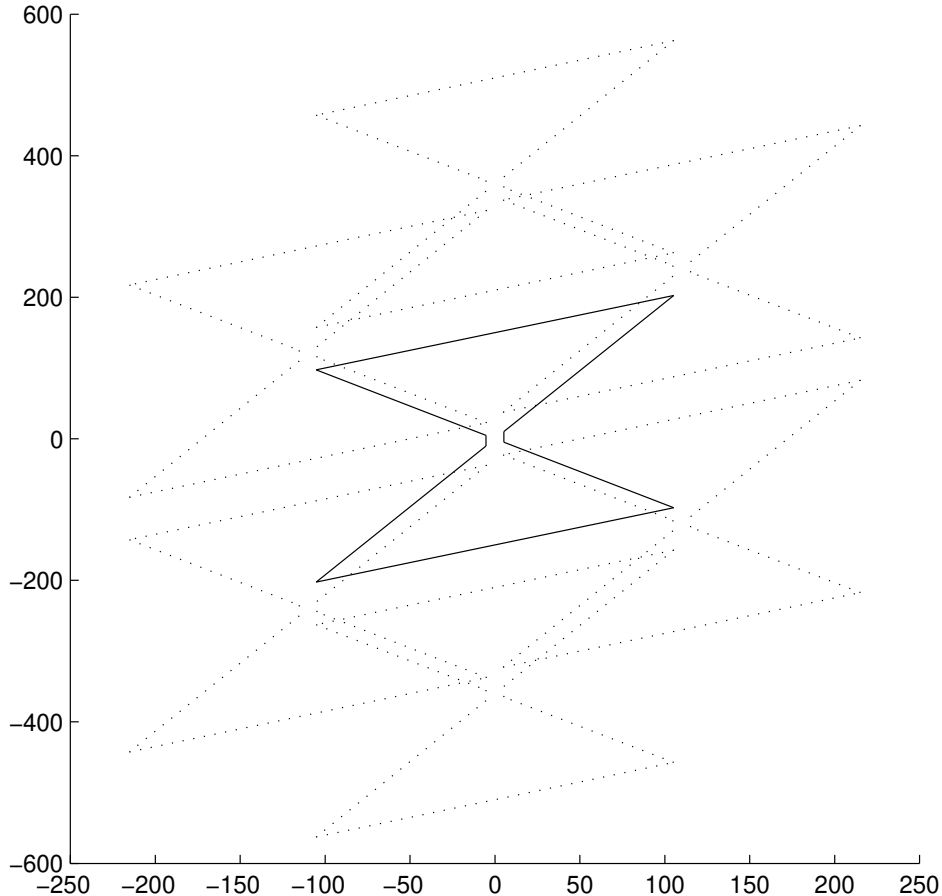

FIGURE 6.   The translated sets $K(\vartheta, b) + \eta$, $\eta \in \mathbf{L}^\perp$ for the efficient lattice in case of $r = 3$, $b = 100$, $\vartheta = 0.95$, $P = 330$, $N = 110$, and $Q = 240$. The increased value of Q compared to Figure 3 leads to overlap of the translated sets and thus aliasing, in spite of sampling more data than with the correct choice $Q = 200$.

The classical sampling theorem can help us understand these experiments at least qualitatively. In Figure 6 we see the translates $K(\vartheta, b) + \eta$, $\eta \in \mathbf{L}^\perp$ for the case corresponding to the lower right reconstruction in Figure 5. We see that increasing Q has led to an overlap of the translates of K and thus undersampling, in spite of having sampled more data. This explains the presence of the artifacts. Increasing

P while leaving both Q and N fixed can also lead to overlap of the translated sets. On the other hand, sampling more data by leaving Q fixed and increasing P and N such that P/N remains constant does not lead to undersampling. In this case the translated sets $K + \eta$ in Figure 3 move further apart from each other in the horizontal direction and remain disjoint.

As our numerical experiment indicated, the efficient lattice shows much greater sensitivity with regard to undersampling in P than the standard lattice. The pattern of overlap of the sets $K + \eta$ provides a qualitative explanation. Figure 7 shows the translated sets $K + \eta$ in case of the standard lattice with $P = 140$, $N = 0$, and $Q = 600$, which partially overlap for this choice of parameters. The effect of such overlap can be investigated with the help of the Poisson summation formula (2.13). Assume we wish to compute an approximation for the Fourier transform $\hat{g}(\zeta)$ from
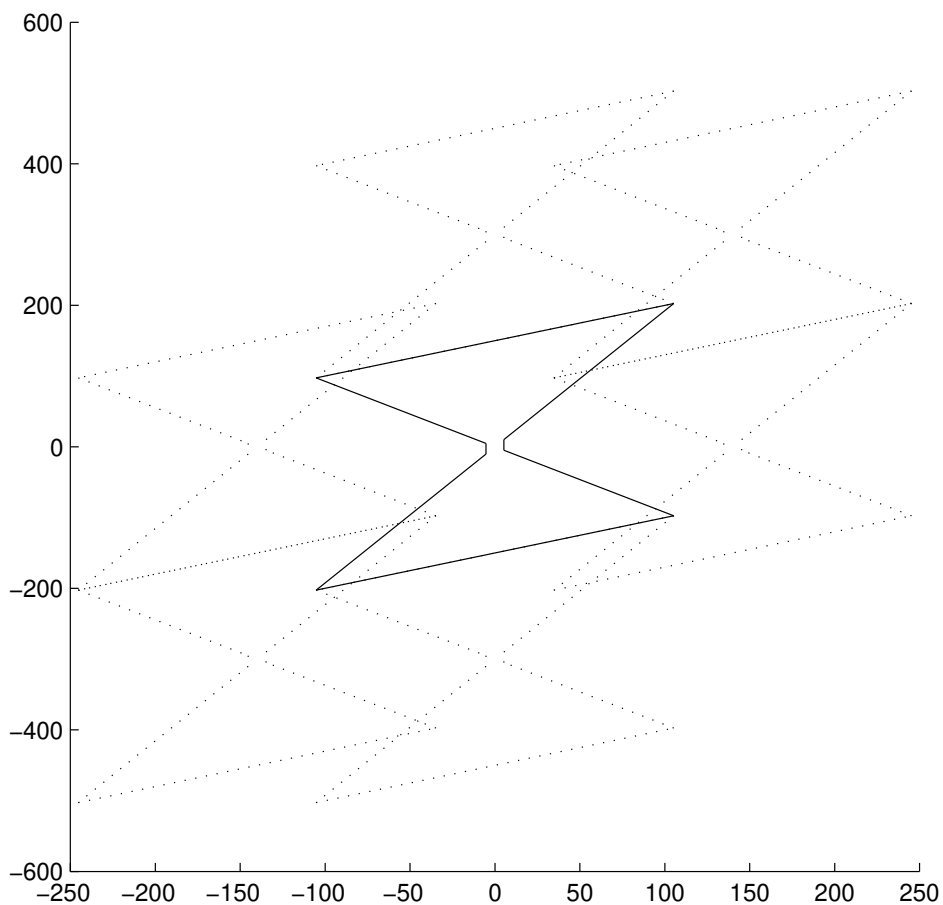

FIGURE 7. The translated sets $K(\vartheta, b) + \eta$, $\eta \in \mathbf{L}^{\perp}$ for the standard lattice with parameters $r = 3$, $b = 100$, $\vartheta = 0.95$, $P = 140$, $N = 0$, and $Q = 600$. The decreased value of P compared to Figure 2 leads to overlap.

the values of g on a sampling lattice $\mathbf{L}$ by means of taking the discrete Fourier transform with respect to $\mathbf{L}$. The result would be $\hat{g}(\zeta) \simeq (1/PQ)\sum_{y\in\mathbf{L}} g(y)e^{-2\pi i\langle y,\zeta\rangle}$, i.e., just the left-hand side of the Poisson summation formula (2.13) for $z = 0$. According to the Poisson summation formula we have

$$\hat{g}(\zeta) \simeq (1/PQ)\sum_{y\in\mathbf{L}} g(y)e^{-2\pi i\langle y,\zeta\rangle} \;=\; \sum_{\eta\in\mathbf{L}^{\perp}} \hat{g}(\zeta+\eta) \;=\; \hat{g}(\zeta) \;+\; \sum_{0\neq\eta\in\mathbf{L}^{\perp}} \hat{g}(\zeta+\eta).$$

If the translated points $\zeta + \eta$ lie outside $K = K(\vartheta, b)$ for $\eta \neq 0$ we may assume that their contribution is small, so that we obtain a good approximation for $\hat{g}(\zeta)$. For $\zeta \in K$ this will be the case if the translated sets $K + \eta$ are disjoint. If the sets $K + \eta$ are not disjoint, there will be non-negligible error terms $\hat{g}(\zeta + \eta)$, with $\zeta + \eta$ lying in the part of K which is overlapped by other translates. In the case of Figure 7 we see that these regions lie well away from the origin. Since f is non-negative (as are almost all functions encountered in tomography) the data function g will be non-negative as well. Hence $|\hat{g}|$ will assume its maximum at the origin and decrease away from the origin. So we can assume that the error resulting from the terms $\hat{g}(\zeta + \eta)$ with $\zeta + \eta$ not close to the origin will be at most moderately large. This gives a qualitative explanation that the standard lattice is not overly sensitive to undersampling with regard to P. By a similar argument we may expect that violating the sampling conditions (3.3) by choosing Q in the excluded range $(1 + \vartheta r)P < Q < 2rb + P$ will in most cases not cause significant artifacts.

The situation is different with the efficient lattice. Figure 8 shows the translated sets $K + \eta$ corresponding to the reconstruction in the lower right of Figure 5. Comparing this to Figure 3 we see that decreasing P from 330 to 300 leads to overlap of K by some of the translated sets, in particular near the origin where $\hat{g}$ is largest. So some of the error terms $\hat{g}(\zeta+\eta)$ will be large, making the efficient lattice considerably more sensitive with regard to undersampling in P than the standard lattice.

A similar discussion has been given for the parallel-beam case in [21], followed by a detailed quantitative error analysis explaining also the location of the artifacts resulting from undersampling. Comparing the two sampling geometries we find that the standard lattice for the fan-beam geometry is more sensitive to undersampling with regard to P than the parallel-beam standard lattice is with regard to undersampling in the variable φ.

3.4. Error analysis of reconstruction algorithms. The most popular tomographic reconstruction algorithm is the so-called filtered backprojection algorithm. It is based on the approximate inversion formula

$$(3.8) \qquad\qquad e * f(x) = \int_0^{2\pi}\int_{\mathbb{R}} k(\langle x,\theta\rangle - s)Rf(\varphi,s)\,ds\,d\varphi$$

where e is an approximate δ-function and the kernel k can be computed from e; see, e.g., [45, p. 102]. The relation (3.8) can be verified by writing $e * f$ as $e * f(x) = \int \hat{e}(\xi)\hat{f}(\xi)e^{i\langle x,\xi\rangle}\,d\xi$, expressing the integral in polar coordinates, and using the relation (2.3); see, e.g., [20].

Discretizing the integrals in equation (3.8) by using the trapezoidal rule yields the filtered backprojection algorithm for the parallel-beam geometry. The appropriate Poisson summation formula furnishes an error estimate. If the sampling
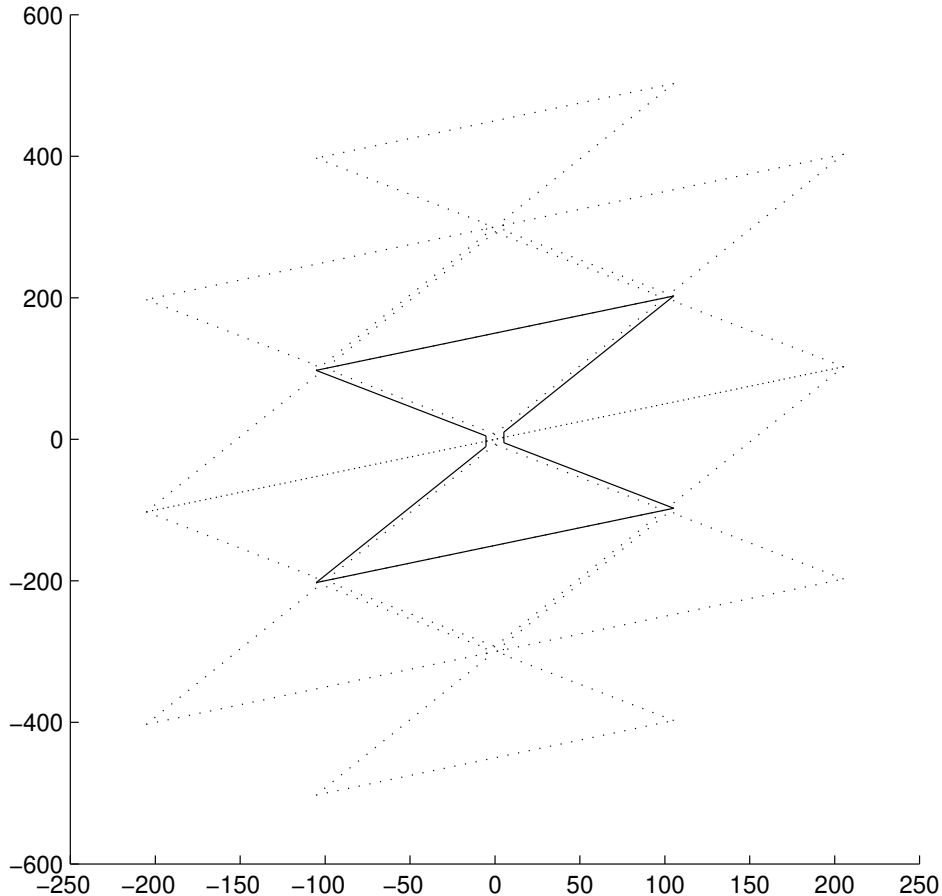
FIGURE 8.   The translated sets $K(\vartheta, b) + \eta$, $\eta \in \mathbf{L}^{\perp}$ for the efficient lattice with parameters $r = 3$, $b = 100$, $\vartheta = 0.95$, $P = 300$, $N = 100$, and $Q = 200$. The decreased value of P compared to Figure 3 leads to overlap.

conditions are satisfied, this error will be small [**38**]. Nevertheless, at first reconstructions with the efficient parallel-beam lattice at full resolution showed large errors. The reason turned out to be an interpolation step in the algorithm. This interpolation is harmless for the standard lattice, but has to be carried out very accurately for the efficient lattice in order to obtain good reconstructions. For details see [**38, 17, 22, 21**]. Convergence rates for the filtered backprojection algorithm were obtained in [**56**] with an approach unrelated to sampling theory.

The filtered backprojection algorithm for the fan-beam geometry is obtained by using the change of variables $\varphi = \alpha + \beta - \pi/2$, $s = r \sin \alpha$ in (3.8) and making additional approximations as mentioned above; see, e.g., [**45**, §V.1.2]. A complete error analysis analogous to the parallel-beam case appears to be still outstanding, but current research may result in considerable progress [**33**]. Kruse [**38**] provided

an error analysis for Marr's algorithm [**43**], which was found to perform superior to direct reconstruction with the fan-beam filtered backprojection algorithm.

4. Exploiting the symmetry: An application of periodic sampling to increase resolution in fan-beam tomography

Periodic sampling sets are unions of shifted copies of a lattice. Such sets are called periodic since they are invariant under shifts with elements of the lattice, since lattices are subgroups. Sampling theorems for periodic sampling sets are more complicated than the classical sampling theorem, but can still be proved using the Poisson summation formula; see, e.g., [**16, 18**]. In this section we briefly describe a very interesting recent development involving periodic sampling. So far we have not yet made use of the symmetry property (2.5). In the parallel-beam case the analogous relation (2.2) is used by choosing lattices which also possess the symmetry, so that only half of the lattice points need to be measured. For special lattices in the fan-beam geometry e.g., the efficient lattice (3.5) introduced in [**46**] this is also the case, but not in general. Izen, Rohler, and Sastry [**32**] discovered a way to exploit the symmetry relation (2.5) to increase resolution. If $Q = 2q$ is even, the (shifted) standard sampling lattice in the (β, α) coordinates is given by

$$
\begin{aligned}
\mathbf{L}_S \;=\; & \{(\beta_j, \alpha_l): \; \beta_j = 2\pi j/P, \;\; \alpha_l = \pi(l+\delta)/q, \\
& j = 0, \ldots, P-1, \;\; l = -q, \ldots, q-1, \;\; \delta \geq 0\}, \;\; Q = 2q.
\end{aligned}
\tag{4.1}
$$

Note the constant shift $\delta\pi/q$ in the α variable. Many scanners use $\delta = 1/4$ to reduce data redundancy. If Df is sampled on the standard lattice (4.1), then using the symmetry (2.5) gives us additional data on a 'reflected lattice'

$$
\mathbf{L}_R = \{(\beta_j + 2\alpha_l + \pi, -\alpha_l) : (\beta_j, \alpha_l) \in \mathbf{L}_S\}.
$$

Since the union $\mathbf{L}_S \cup \mathbf{L}_R$ is in general not a lattice (or shifted lattice) itself, the classical sampling theorem cannot be applied. In addition, since $\mathbf{L}_R$ differs from $\mathbf{L}_S$ by more than a constant shift, $\mathbf{L}_S \cup \mathbf{L}_R$ is a union of two different lattices, so a periodic sampling theorem which handles sampling sets which are unions of shifted copies of the same lattice does at first glance also not apply. However, Izen et al. [**32**] discovered that $\mathbf{L}_S \cup \mathbf{L}_R$ is a union of $2q/\gcd(P, q)$ shifted copies of the smaller lattice

$$
\mathbf{L}_P = \{(2\pi j/P, \; \pi l/\gcd(P, q)), \; j = 0, \ldots, P-1, \; |l| \leq \gcd(P, q)\}.
$$

While Izen, Rohler, and Sastry used a different approach to reconstruction, their discovery makes it possible to apply the periodic sampling theorem and interpolation algorithms of [**18**]. This is somewhat more complicated but also more general than the approach of [**32**]. A first demonstration has recently been given by Mitchell [**44**]. While normally doubling the resolution would require four times the data, using the reflected data allows us to achieve twice the resolution achievable with $\mathbf{L}_S$ alone by only having to double the number P of source positions. According to [**32**] this also overcomes the following problem, related to the beams of finite width mentioned by Cormack in the quote at the beginning of this article. It can be shown that the natural band-limiting of the data caused during the measurement process by the averaging over the finite detector width d (i.e., by using beams of finite width instead of measuring line integrals) corresponds to a maximum frequency of approximately $2\pi/d$; cf. [**35**, §5.1.2]. On the other hand, the highest sampling rate in the α variable occurs when the detectors are adjacent, so it is equal to d. Hence

according to Theorem 2.2 the highest resolvable frequency would be $b = \pi/d$, only half as large as the band-width of the measured data. Using the reflected data as described above now allows to achieve the full resolution.

5. Conclusions

This article has given an introduction to the use of sampling theory in tomography using the example of the two-dimensional fan-beam geometry. The approach taken here involved a change of variables so that existing theory and software [**18**] for sampling on the torus group $\mathbb{T}^2$ could be used. A parameterization of all sampling lattices was given. The commonly used standard lattice and an efficient lattice similar to the one of [**46**] were given special attention, including a complete set of sampling conditions for the standard lattice.

Numerical experiments were presented, indicating that unlike the parallel-beam case, a direct application of the fan-beam filtered backprojection algorithm does give suboptimal, and in case of the efficient lattice unacceptable, results. On the other hand, using the sampling theorem to first bandlimit the data to the set $K(\vartheta, b)$ and then interpolating it to a dense lattice prior to reconstruction yields accurate reconstructions, at least for a smooth test object.

A qualitative explanation of artifacts resulting from undersampling was given with results similar to the parallel-beam case, the most significant difference being the somewhat higher sensitivity of the fan-beam standard lattice with regard to undersampling in the number of source positions. Finally, a new way to exploit the symmetry of the data to increase resolution was reviewed.

Two practically important issues left out of the preceding discussion are functions with discontinuities and the effect of noise. Discontinuities cause a slower decay of the Fourier transform and thus the assumption of an essential bandwidth b is less well satisfied. A common way to deal with the resulting artifacts is to filter the data prior to reconstruction. The trade-off is that this gives up some of the higher resolution gained by efficient sampling. Noise in the data is similarly more critical when reconstructing at high resolution with sparsely sampled data. One way to deal with this problem is to denoise the reconstructed image with a denoising method that preserves edges, such as the method of Rudin-Osher-Fatemi [**58**] based on minimizing the total variation. Recently Hass [**27**] has demonstrated that such denoising may remove the increased effects of noise and still retain somewhat higher resolution.

We conclude by giving a list of examples of areas where sampling theory and tomography have interacted and stimulated each other. An area of increasing current interest is sampling in three-dimensional tomography. The list below is by no means complete but is meant to provide interested readers with an opportunity for further study.

5.1. Examples for the interaction of sampling theory and tomography. A brief overview of how sampling theory and tomography have interacted and stimulated each other may contain at least the themes and topics listed below.

5.1.1. *Applications of the Classical Sampling Theorem.*

- *Identification of efficient sampling lattices in 2D and 3D.* The goal is to obtain a desired resolution with a minimum number of measurements. See, e.g., [**11, 12, 13, 14, 19, 31, 40, 45, 46, 47, 48, 49, 55**].

- *Qualitative understanding of artifacts.* The classical sampling theorem permits a qualitative understanding of artifacts caused by aliasing from undersampling; see, e.g., [**17, 21, 31**].
- *Error analysis of reconstruction algorithms.* The Poisson summation formula connects sampling theory to the error analysis of the filtered backprojection algorithm; see, e.g., [**17, 21, 22, 33, 38, 39, 45, 49**]. For results on algebraic algorithms see [**10, 36**].

5.1.2. *Research in Sampling Theory stimulated by CT.* Different data acquisition geometries in tomography stimulate interest in:

- *Sampling theorems where the sampling set is not a lattice.*
  - *Multidimensional periodic sampling sets.* Here the sampling set is a union of several cosets of a lattice. See [**16, 18**].
  - *Non-periodic sampling on unions of shifted lattices* [**2, 59**].
  - *Non-uniform sampling.* Here the sampling set has no structure which could be exploited with the Poisson summation formula. Examples include polar or spiral sampling in Fourier space; see, e.g., [**1, 5, 23, 53**].
- *An estimate for the aliasing error sharper than (2.15)* [**19**].
- *A unified mathematical framework.* Many applications of sampling can be unified in the simple and elegant framework of Fourier analysis on locally compact abelian groups; see,e.g., [**2, 15, 18, 37**].

5.1.3. *Applications of periodic sampling in CT.*

- *Additional efficient 2D sampling schemes* [**9, 16**].
- *'Preferred pitch' in 3D helical CT* [**25, 57**].
- *Higher resolution in 2D fan-beam CT* [**32**].

5.1.4. *Applications of non-periodic sampling.*

- *Higher resolution in 2D fan-beam CT* [**25**].

References

[1] A. Aldroubi and K. Gröchenig, *Nonuniform sampling and reconstruction in shift-invariant spaces*, SIAM Review **43** (2001), 585–620.

[2] H. Behmard and A. Faridani, *Sampling of bandlimited functions on unions of shifted lattices*, J. Fourier Anal. Appl. **8** (2002), 43–58.

[3] J. J. Benedetto and P. J. S. G. Ferreira (eds.), *Modern Sampling Theory: Mathematics and Applications*, Birkhäuser, Boston, 2001.

[4] J. J. Benedetto and A. I. Zayed (eds.), *Sampling, Wavelets, and Tomography*, Birkhäuser, Boston, 2004.

[5] M. Bourgeois, F. T. A. W. Wajer, D. van Ormondt, and D. Graveron-Demilly, *Reconstruction of MRI images from non-uniform sampling and its application to intrascan motion correction in functional MRI*, in [**3**], pp. 343–363.

[6] G. H. Bradley, *Algorithms for Hermite and Smith normal matrices and linear Diophantine equations*, Math. Comp. **25** (1971), 897–907.

[7] P. L. Butzer, W. Splettstößer and R. L. Stens, *The sampling theorem and linear prediction in signal analysis*, Jber. d. Dt. Math.-Verein. **90** (1988), 1–70.

[8] A. M. Cormack, *Sampling the Radon transform with beams of finite width*, Phys. Med. Biol. **23** (1978), 1141–1148.

[9] L. Desbat, *Efficient sampling on coarse grids in tomography*, Inverse Problems **9** (1993), 251–269.

[10] L. Desbat, *Algebraic reconstructions from efficient sampling schemes in tomography*, Computerized Tomography (M.M. Lavrent'ev, ed.), VSP, Utrecht, 1995, pp. 124–137.

[11] L. Desbat, *Echantillonnage paralléle efficace en tomographie 3D*, C.R. Acad. Sci. Paris, Sërie I, **324** (1997), 1193-1199.

[12] L. Desbat, *Interpolation of lacking data in tomography*, Proceedings of SampTA 2001, Intern. Conference on Sampling Theory and Applications, Orlando, FL, 2001, pp. 123–128.

[13] L. Desbat, S. Roux, P. Grangeat, and A. Koenig, *Sampling conditions of 3D parallel and fan-beam x-ray CT with application to helical tomography*, Phys. Med. Biol. **49** (2004), 2377–2390.

[14] L. Desbat and C. Mennessier, *Efficient sampling of the rotation invariant Radon transform*, in [**3**], pp. 365–377.

[15] M. M. Dodson and M. G. Beaty, *Abstract harmonic analysis and the sampling theorem*, in [**30**], pp. 233–265.

[16] A. Faridani, *An application of a multidimensional sampling theorem to computed tomography*, Contemporary Mathematics, **113** (1990), 65–80.

[17] A. Faridani, *Reconstructing from efficiently sampled data in parallel-beam computed tomography*, Inverse Problems and Imaging (G.F. Roach, ed.), Pitman Research Notes in Mathematics Series, vol. 245, Longman, 1991, pp. 68–102.

[18] A. Faridani, *A generalized sampling theorem for locally compact abelian groups*, Math. Comp. **63** (1994), 307–327.

[19] A. Faridani, *Sampling in parallel-beam tomography*, Inverse Problems, Tomography, and Image Processing (A. G. Ramm, ed.), Plenum, New York, 1998, pp. 33–53.

[20] A. Faridani, *Introduction to the Mathematics of Computed Tomography*, Inside Out: Inverse Problems and Applications (G. Uhlmann, ed.), MSRI Publications, vol. 47, Cambridge University Press, 2003, pp. 1–46.

[21] A. Faridani, *Sampling theory and parallel-beam tomography*, in [**4**], pp. 225–254.

[22] A. Faridani and E. L. Ritman, *High-resolution computed tomography from efficient sampling*, Inverse Problems **16** (2000), 635–650.

[23] K. Fourmont, *Non-equispaced fast Fourier transforms with applications to tomography*, J. Fourier Anal. Appl. **9** (2003), 431–450.

[24] G. B. Folland, *Real Analysis*, Wiley, New York, 1984.

[25] L. A. Gratton, *Nonuniform Sampling Problems in Computed Tomography*, Ph.D. thesis, Dept. of Mathematics, Oregon State University, 2005.

[26] K. Gröchenig, *Aspects of Gabor analysis on locally compact abelian groups*, Gabor Analysis and Algorithms (H. G. Feichtinger and T. Strohmer, eds.), Birkhäuser, Boston, 1998, pp. 211–231.

[27] R. A. Hass, *De-noising tomography images through bounded variation*, M.S. paper, Dept. of Mathematics, Oregon State University, 2005.

[28] J. R. Higgins, *Five short stories about the cardinal series*, Bull. Amer. Math. Soc. **12** (1985), 45–89.

[29] J. R. Higgins, *Sampling Theory in Fourier and Signal Analysis: Foundations*, Clarendon Press, Oxford, 1996.

[30] J. R. Higgins and R. L. Stens (eds), *Sampling Theory in Fourier and Signal Analysis: Advanced Topics*, Clarendon Press, Oxford, 1999.

[31] T.-C. Hsung and D. P. K. Lun, *New sampling scheme for region-of-interest tomography*, IEEE Trans. Signal Processing **48** (2000), 1154–1163.

[32] S. H. Izen, D. P. Rohler, and K.L.A Sastry, *Exploiting symmetry in fan-beam CT: Overcoming third generation undersampling*, SIAM J. Appl. Math. **65** (2005), 1027–1052.

[33] S. H. Izen, *An analysis of the fan beam CT reconstruction kernel*, talk presented at the Special Session on Radon Transform and Inverse Problems, AMS National Meeting, Atlanta, January 2005.

[34] A. J. Jerri, *The Shannon sampling theorem - its various extensions and applications: a tutorial review*, Proc. IEEE **65** (1977), 1565–1596.

[35] A. C. Kak and M. Slaney, *Principles of computerized tomographic imaging*, IEEE Press, New York, 1988.

[36] W. Klaverkamp, *Tomographische Bildrekonstruktion mit direkten algebraischen Verfahren*, Ph.D. thesis, Fachbereich Mathematik, Westfälische Wilhelms-Universität Münster, Germany, 1991.

[37] I. Kluvanek, *Sampling theorem in abstract harmonic analysis*, Mat. Casopis Sloven. Akad. Vied, **15** (1965), 43–48.

[38] H. Kruse, *Resolution of reconstruction methods in computerized tomography*, SIAM J. Sci. Stat. Comput. **10** (1989), 447–474.

[39] R. M. Lewitt, R. H. T. Bates, and T .M. Peters, *Image reconstruction from projections: II: Modified back-projection methods*, Optik **50** (1978), 85–109.

[40] A. G. Lindgren and P. A. Rattey, *The inverse discrete Radon transform with applications to tomographic imaging using projection data*, Advances in Electronics and Electron Physics **56** (1981), 359–410.

[41] R. J. Marks II, *Introduction to Shannon Sampling and Interpolation Theory*, Springer, New York, 1991.

[42] R. J. Marks II (ed.), *Advanced Topics in Shannon Sampling and Interpolation Theory*, Springer, New York, 1993.

[43] R. B. Marr, *On the reconstruction of a function on a circular domain from a sampling of its line integrals*, J. Math. Anal. Appl. **45** (1974), 357–374.

[44] N. Mitchell, *Multi-dimensional sampling in fan beam tomography*, M.S. paper, Dept. of Mathematics, Oregon State University, 2005.

[45] F. Natterer, *The Mathematics of Computerized Tomography*, Wiley, 1986.

[46] F. Natterer, *Sampling in fan-beam tomography*, SIAM J. Appl. Math. **53** (1993), 358–380.

[47] F. Natterer, *Sampling and resolution in CT*, Computerized Tomography (M.M. Lavrent'ev, ed.), VSP, Utrecht, 1995, pp. 343–354.

[48] F. Natterer, *Resolution and reconstruction for a helical CT scanner*, Technical Report 20/96-N, Fachbereich Mathematik, Universität Münster, Germany, 1996.

[49] F. Natterer and F. Wuebbeling, *Mathematical Methods in Image Reconstruction*, SIAM, Philadelphia, 2001.

[50] H. Niederreiter, *Random Number Generation and Quasi-Monte Carlo Methods*, SIAM, Philadelphia, 1992.

[51] M. Newman, *Integral Matrices*, Academic Press, 1972.

[52] V. P. Palamodov, *Localization of harmonic decomposition of the Radon transform*, Inverse Problems **11** (1995), 1025–1030.

[53] D. Potts and G. Steidl, *Fourier reconstruction of functions from their nonstandard sampled Radon transform*, J. Fourier Anal. Appl. **8** (2002), 513–533.

[54] E. T. Quinto, *An introduction to x-ray tomography and Radon transforms*, this volume.

[55] P. A. Rattey and A. G. Lindgren, *Sampling the 2-D Radon transform*, IEEE Trans. Acoust. Speech Signal Processing **29** (1981), 994–1002.

[56] A. Rieder and A. Faridani, *The semi-discrete filtered backprojection algorithm is optimal for tomographic inversion*, SIAM J. Num. Anal. **41** (2003), 869–892.

[57] P. J. La Riviere and X. Pan, *Pitch dependence of longitudinal sampling and aliasing effects in multi-slice helical computed tomography (CT)*, Phys. Med. Biol. **47** (2002), 2797–2810.

[58] L.I. Rudin, S. Osher, and E. Fatemi, *Nonlinear total variation based noise removal algorithms*, Phys. D **60** 1-4 (1992), 259–268.

[59] D. Walnut *Nonperiodic sampling of bandlimited functions on unions of rectangular lattices*, J. Fourier Anal. Appl. **2** (1996), 435–452.

[60] A. I. Zayed, *Advances in Shannon's Sampling Theory*, CRC Press, Boca Raton, Florida, 1993.

DEPARTMENT OF MATHEMATICS, OREGON STATE UNIVERSITY, CORVALLIS, OREGON, 97331
E-mail address: faridani@math.oregonstate.edu